



## Cu-Pd alloy nanoparticles as highly selective catalysts for efficient electrochemical reduction of CO<sub>2</sub> to CO



Yeongdong Mun<sup>a,1</sup>, Seunghyun Lee<sup>a,1</sup>, Ara Cho<sup>a</sup>, Seongbeen Kim<sup>a</sup>, Jeong Woo Han<sup>a,\*</sup>, Jinwoo Lee<sup>b,\*</sup>

<sup>a</sup> Department of Chemical Engineering, Pohang University of Science and Technology (POSTECH), 77 Cheongam-ro, Nam-gu, Pohang 37673, Republic of Korea

<sup>b</sup> Department of Chemical and Biomolecular Engineering, Korea Advanced Institute of Science and Technology (KAIST), 291 Daehak-ro, Yuseong-gu, Daejeon 34141, Republic of Korea

### ARTICLE INFO

#### Keywords:

Electrochemical CO<sub>2</sub> reduction  
Electrocatalyst  
Nanoparticle  
Copper  
Palladium

### ABSTRACT

Although a copper catalyst has very interesting properties in CO<sub>2</sub> electroreduction reaction (CO<sub>2</sub>RR), the high overpotential of this reaction and low selectivity of the catalyst for a single product are major hindrances to catalyst commercialization. In this work, monodisperse Cu-Pd nanoparticles (NPs) with various compositions are synthesized using the colloidal method. These NPs show a totally different catalytic performance than bulk Cu catalysts. Alloying Cu with Pd suppresses hydrocarbon production on the alloy NP catalyst surface. NPs with a 1:1 Cu-Pd ratio show the best catalytic activity for the conversion of CO<sub>2</sub> to CO. At -0.9 V (vs. RHE), 87% CO Faradaic efficiency is achieved, as well as a high noble metal mass activity of 47 mA mg<sub>Pd</sub><sup>-1</sup> for CO production. Density functional theory calculations suggest that the energy barrier to the CO\* protonation step is increased when Pd is alloyed with Cu; this increase suppresses the reduction of CO<sub>2</sub> to hydrocarbons. This result is a significant advance toward selective electrochemical reduction of CO<sub>2</sub>.

### 1. Introduction

Reducing carbon dioxide (CO<sub>2</sub>) emissions is crucial for the sustainability of human society [1,2]. The greenhouse effect, induced by a high concentration of CO<sub>2</sub> in the atmosphere, has resulted in unpredictable climate changes. There are two ways to reduce the CO<sub>2</sub> concentration in the atmosphere. One is to develop new and renewable energy that is obtained without CO<sub>2</sub> production [3,4]. The other is to capture the produced CO<sub>2</sub> gas before emission [5,6]. Because CO<sub>2</sub> is produced inevitably in some industries (e.g., the steel industry), and the energy supply from new renewable energy sources is not yet stable, the development of technology for the latter route is important. The utilization of captured CO<sub>2</sub> (CCU) is a strategy to exploit CO<sub>2</sub> that has been captured by industrial CO<sub>2</sub> emission capture technology [7,8]. CCU methods include mineralization, biological conversion, and chemical conversion [9–11]. CCU increases the benefits of CO<sub>2</sub> mitigation by using CO<sub>2</sub> as a feedstock for valuable processes. The CCU process has advantages not only including reducing CO<sub>2</sub> emissions (where the total carbon emission of the overall process is less than the reduction in CO<sub>2</sub> through the process) but also using CO<sub>2</sub> as a carbon source of readily available feedstock, which creates economic values [11–13].

The electrochemical reduction of CO<sub>2</sub> (CO<sub>2</sub>RR) is a promising way to utilize CO<sub>2</sub> as a resource for the production of useful chemicals [14,15]. CO<sub>2</sub>RR can store excess energy from renewable energy sources in the form of chemicals instead of electric power [16]. However, the CO<sub>2</sub>RR has a high overpotential, which decreases the energy efficiency of CO<sub>2</sub>RR cells significantly. Although the thermodynamically calculated equilibrium reduction potential is not high (CO: -0.10 V, CH<sub>4</sub>: 0.17 V, HCOOH: -0.02 V, C<sub>2</sub>H<sub>4</sub>: 0.08 V, and C<sub>2</sub>H<sub>5</sub>OH: 0.09 V vs. SHE), the onset potential at which each chemical starts to be produced is much more negative than the theoretical value. To reduce this high overpotential, highly efficient catalysts must be designed [17–19].

Recently, a variety of metal catalysts including Au, Ag, Pd, Cu, and Sn has been studied, and their nanostructured materials have also been employed to enhance the catalytic activity further [20–25]. In particular, Cu catalysts are inexpensive and can produce hydrocarbons (e.g., CH<sub>4</sub>, CH<sub>3</sub>OH, C<sub>2</sub>H<sub>4</sub>, and C<sub>2</sub>H<sub>5</sub>OH) from CO<sub>2</sub> by a multi-electron transfer process [26,27]. The production of hydrocarbons requires at least eight individual reaction steps involving proton and electron transfer. The protonation of adsorbed CO (CO\*) is the key step in determining the overpotential of hydrocarbon production, and the Cu surface provides the most appropriate binding energies for intermediates of the CO<sub>2</sub>RR

\* Corresponding authors.

E-mail addresses: [jwhan@postech.ac.kr](mailto:jwhan@postech.ac.kr) (J.W. Han), [jwlee1@kaist.ac.kr](mailto:jwlee1@kaist.ac.kr) (J. Lee).

<sup>1</sup> These authors contributed equally to this work.

to minimize the energy barrier to this step [28].

However, use of Cu as a catalyst for the CO<sub>2</sub>RR is disadvantageous because it produces a mixture of gases, which must be separated and purified; to avoid this costly necessity, the catalytic behavior of Cu catalyst must be modified so that it yields one valuable product with high selectivity. The use of alloy nanoparticles (NPs) is a promising strategy to modify the catalytic properties. Alloying can change the electronic and geometric structures of the metal surface, which are closely related to the catalytic properties [29–33]. In terms of electronic structure, d-band center which affects the intermediate binding energy could be controlled by varying atomic ratio in alloy. In point of geometric effects, alloying changes surface strain and binding modes of intermediates, which could affect the binding energy of specific intermediates regardless of the scaling relations [34]. The use of NPs enables a sensitive analysis of how the composition affects the alloyed catalyst. The colloidal synthesis of NPs is highly tunable, so NPs of various compositions can be synthesized with similar shapes and sizes [35–37]. In addition, the high surface-to-volume ratio of the NPs is advantageous for achieving a high catalytic reaction rate.

In this study, we synthesized NPs of Cu-Pd alloyed catalysts in various compositions to tune the selectivity of CO<sub>2</sub>RR on Cu catalysts. The catalytic behavior of the Cu NPs was totally changed by Pd alloying [38,39]. Alloying Pd to Cu would be beneficial for the enhancement of CO production due to relatively strong CO binding energy of Pd, which increases the potential barrier of CO\* protonation step [40]. Furthermore, Cu-Pd alloy was predicted to have low activity toward competitive hydrogen evolution reaction (HER) [41]. The Faradaic efficiencies of Cu-Pd alloy NPs for CO<sub>2</sub>RR to CO were much higher than those of the Cu NPs. NPs with a 1:1 ratio of Cu-Pd showed the best catalytic performance for the conversion of CO<sub>2</sub> to CO. At -0.9 V (vs. RHE), the CuPd NPs showed 87% CO Faradaic efficiency and a high noble metal mass activity of 47 mA mg<sub>Pd</sub><sup>-1</sup> for CO production. This noble metal mass activity is much higher than those of previously reported Pd-based catalysts. This is highly advantageous in terms of economic feasibility. In addition, the Cu-Pd alloy NP catalysts produced no hydrocarbons. This drastically different catalytic performance was confirmed by our density functional theory (DFT) calculations, which suggested that the alloying of Cu and Pd increases the energy barrier to the CO\* protonation step; this increase hinders the further reduction of CO\* to hydrocarbons.

## 2. Experimental

### 2.1. Sample preparation

#### 2.1.1. Synthesis of monodisperse CuPd<sub>x</sub> NPs

For CuPd NPs, Cu(acac)<sub>2</sub> (0.052 g, 0.2 mmol), PdCl<sub>2</sub> (0.036 g, 0.2 mmol), and oleylamine (10 mL) were loaded into a 25-mL three-necked flask while stirring. The mixture was heated under a N<sub>2</sub> atmosphere to 100 °C at 2 °C min<sup>-1</sup> and held at 100°C for 30 min. Then, the mixture was heated to 250°C at 10 °C min<sup>-1</sup> and incubated at 250°C for 30 min, generating a black suspension of NPs. The suspension was cooled to room temperature (RT), and then ethanol was added to precipitate the synthesized NPs. The NPs were washed three times with 50-mL portions of acetone by centrifugation. For other compositions, the ratio of [Cu(acac)<sub>2</sub>] to PdCl<sub>2</sub> was adjusted. The synthesized NPs were redispersed in hexane.

#### 2.1.2. Synthesis of monodisperse Pd nanoparticles

Pd NPs with an average particle size of 3 nm (Pd-3 NPs) were synthesized by the reported method [42]. Pd (acac)<sub>2</sub> (0.1 g, 0.33 mmol) and 1 mL of trioctylphosphine (TOP) were mixed in an Ar atmosphere and then stirred for 2 h. Then, 9 mL of TOP was added to the solution, and it was purged with Ar. In an Ar atmosphere, the solution was heated to 300 °C at 2 °C min<sup>-1</sup> and held at 300 °C for 30 min. The solution was cooled to RT, then the Pd-3 NPs were precipitated by the addition

of ethanol and collected by centrifugation (6000 rpm). Pd NPs with average particle sizes of 5 nm (Pd-5 NPs) and 7 nm (Pd-7 NPs) were prepared similarly, except that 2 mL TOP was used to obtain Pd-5 NPs and 1.4 mL TOP was used to obtain Pd-7 NPs.

#### 2.1.3. Synthesis of monodisperse Cu nanoparticles

Cu NPs were synthesized using a modification of the same method [43]. Cu(acac)<sub>2</sub> (0.8 g, 3 mmol) was dissolved in oleylamine (10 mL). After purging with Ar, the solution was rapidly heated to 280 °C at 15 °C min<sup>-1</sup>, then held at 280 °C for 1 h. The solution was cooled to RT, then Cu NPs was precipitated by adding ethanol, then collected by centrifugation (6000 rpm).

#### 2.1.4. Synthesis of carbon-supported nanoparticle catalysts (20% loading)

Hexane dispersion (50 mL) of 25 mg of CuPd, Cu3Pd, CuPd3, Cu, or Pd NPs (3 nm, 5 nm, 7 nm) was mixed with 100 mg carbon black (Vulcan XC-72R) and sonicated for 40 min. Then, the mixture was washed with ethanol by centrifugation and redispersed in 20 mL of hexane, followed by drying at 85°C. Finally, the catalysts were heated to 185°C for 6 h to remove residual surfactant from the nanoparticles.

## 2.2. Material characterization

The crystal structures of all NP types were investigated by X-ray diffraction (XRD) (Bruker D8 Advance, Cu K $\alpha$  radiation). The size, morphology, and d-spacing of samples were confirmed using transmission electron microscopy (TEM, JEM-1011 JEOL Ltd.) and high-resolution (HR)-TEM (JEOL JEM-2100). The high-angle annular dark-field – scanning transmission electron microscope (HAADF-STEM) images and STEM combined with energy dispersive X-ray spectroscopy (STEM-EDS) data were corrected using JEOL ARM200 F microscope operated at 200 kV. The cross-section of the catalysts loaded carbon paper was investigated by scanning electron microscopy (SEM) (S-4200 field emission microscope, Hitachi). The catalyst loading was measured by thermogravimetric analysis (TGA) (Hitachi STA7300) and inductively coupled plasma spectroscopy-optical emission spectroscopy (ICP-OES) (Shimadzu ICPE-9000).

## 2.3. Electrochemical measurements

Current collectors for the working electrode were prepared by mixing a slurry of carbon black (Vulcan XC-72R) and polytetrafluoroethylene (PTFE) binder (PTFE content: 15 wt%), which was sprayed on commercial carbon paper (Toray TGP-H-060) with a loading of 1 mg cm<sup>-2</sup>. Then, 10 mg of the NPs on the carbon support (NP/C) and a Nafton solution (25  $\mu$ L) were dispersed in IPA (1 mL), and the mixture was sonicated for 1 h. The well-dispersed catalyst ink was drop-cast onto the carbon-coated carbon paper.

All electrochemical measurements were performed in our customized electrochemical setup (Fig. S1). The cell had two compartments that were separated by an anion exchange membrane (Soleimion AMV, AGC in Japan). The counter electrode was a Pt mesh, and the reference electrode was Ag/AgCl (saturated KCl). Both cells were filled with the electrolyte (0.1 M KHCO<sub>3</sub>) and purged continuously with CO<sub>2</sub> (10 mL min<sup>-1</sup>). After purging CO<sub>2</sub> into each compartment for 20 min, chronomperometry was performed at each potential for 20 min.

## 2.4. Product quantification

The gas product flow was injected through switching valves (6-port valves) into a gas chromatograph (GC) (Agilent 7890B), which is equipped with a flame ionization detector (FID) with a methanizer for CO and hydrocarbons, and a thermal conductivity detector (TCD) for H<sub>2</sub>. The samples were separated by HP-5 capillary column with argon as a carrier gas. The FID detected CO near 2.5 min, CH<sub>4</sub> near 5 min, CO<sub>2</sub> near 9 min, and C<sub>2</sub>H<sub>4</sub> near 16 min, and the TCD detected H<sub>2</sub> near 1 min

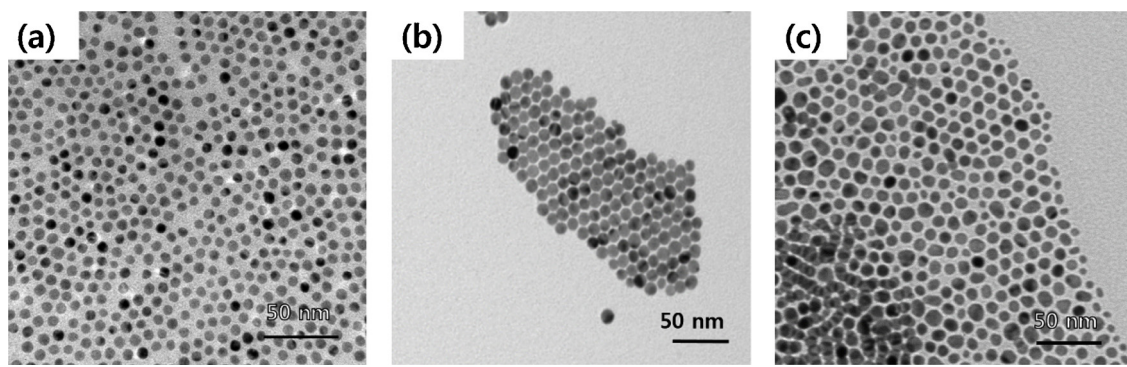


Fig. 1. TEM images of Cu-Pd alloy NPs: (a) Cu<sub>3</sub>Pd, (b) CuPd, and (c) CuPd<sub>3</sub>.

(Fig. S2).

The Faradaic efficiency,  $FE_X$ , of each product was calculated using Eq. (1),

$$FE_X = \frac{n\alpha_X vF \times \text{peak area}}{IRT}, \quad (1)$$

where  $n$  is the number of the electrons consumed when one molecule of CO<sub>2</sub> is converted to X,  $\alpha_X$  is a conversion factor calculated from the calibration of the GC with a standard gas (N<sub>2</sub> base, 1 mol% of H<sub>2</sub>, CO, CO<sub>2</sub>, CH<sub>4</sub>, or C<sub>2</sub>H<sub>4</sub>),  $v$  is the gas flow rate of the working cell (10 mL min<sup>-1</sup>), F is the Faraday constant,  $I$  is the total current measured when the analyte sample is injected, and  $R$  is the gas constant.

Liquid products were analyzed by <sup>1</sup>H-NMR (Bruker AV-500) using dimethylsulfoxide (DMSO) (for ethanol) and phenol (for formate) as internal standards (Fig. S3a). Before quantitative analysis, we determined calibration curve with various concentrations (0, 1, 2, 3, 4, and 5 mM) of ethanol and formate (Fig. S3b). Both standard curves showed a linear relationship. To prepare the analyte sample, 1 mL of sample solution after electrolysis was mixed with 50  $\mu$ L of an internal standard solution (5 mM DMSO + 25 mM phenol). Then, 150  $\mu$ L of the mixture was mixed with 450  $\mu$ L of D<sub>2</sub>O for a quantitative NMR analysis.  $FE_X$  was calculated from the charge consumed by each product divided by the total charge.

## 2.5. Computational details

Spin-polarized DFT calculations were performed with the Vienna *ab initio* simulation package (VASP) using the projector augmented wave method [44–47]. The exchange-correlation energies were treated using the Perdew–Burke–Enznerhof (PBE) functional of the generalized gradient approximation (GGA) [48,49]. A plane-wave basis set with a cut-off energy of 600 eV was used. The Brillouin zone was sampled using Monkhorst–Pack 3  $\times$  3  $\times$  1  $k$ -point meshes. Methfessel–Paxton smearing was employed with a width of 0.2 eV [49]. Geometries relaxation was carried out until the forces on unconstrained atoms were less than 0.3 eV Å<sup>-1</sup>. The optimized lattice constants of 3.635 and 3.800 Å were obtained for Cu and CuPd, respectively. The periodic surface models of Cu(211) and CuPd(211) were chosen to represent the step surfaces using four atomic layers with (1  $\times$  4) and (1  $\times$  2) surface unit cells, respectively. The bottom two layers were fixed with vacuum space of 15 Å. Based on the method proposed by Nørskov et al. [50,51], the Gibbs free energy change was calculated using Eq. (2),

$$\Delta G = \Delta E + \Delta ZPE + \Delta \int C_p dT - T\Delta S + \Delta G_{\text{sol}} - eU, \quad (2)$$

where  $\Delta E$  is the reaction energy obtained from the DFT calculations,  $\Delta ZPE$  is the zero-point energy,  $C_p$  is the heat capacity, and  $S$  is the entropy.  $T$  was set to 291.65 K.  $\Delta G_{\text{sol}}$  is the correction energy obtained from the Poisson–Boltzmann implicit solvation model with a dielectric constant  $\epsilon = 80$  for water [52], and  $eU$  is the free energy of the proton–electron pair, where  $e$  is the transferred charge and  $U$  is the

electrode potential relative to the standard hydrogen electrode (SHE) [51]. In this calculation, we used the correction energy of + 0.13 eV for gas-phase CO<sub>2</sub> molecule [50]. The binding energy ( $E_B$ ) of intermediates on the surfaces was calculated using Eq. (3),

$$E_B = E_{C_xO_yH_z} - E_{\text{slab}} - xE_C - yE_H - zE_O, \quad (3)$$

where  $E_{C_xO_yH_z}$  is the total energy of the intermediates adsorbed on the metal surfaces,  $E_{\text{slab}}$  is the total energy of the slab,  $E_C$  is the energy of a C atom referenced to graphene,  $E_H$  is the energy of a H atom obtained from 1/2  $E_{H_2}$  (g), and  $E_O = E_{H_2O} - E_{H_2}$  is the energy of an O atom.

## 3. Results and discussion

### 3.1. Synthesis and analysis of the catalysts

Cu and Pd alloy NPs were synthesized by a general colloidal synthesis using oleylamine as reducing agent, surfactant, and solvent [43,53]. Copper acetylacetone and anhydrous palladium chloride were used as metal precursors, and the compositions of the NPs were controlled by changing the feeding ratio of the precursors. The average diameters of the synthesized alloy NPs were 6.6 nm (Cu<sub>3</sub>Pd NPs), 6.8 nm (CuPd NPs), and 7.7 nm (CuPd<sub>3</sub> NPs), and all NPs had a spherical shape (Fig. 1). For comparison, monometallic Cu and Pd NPs were also synthesized with similar sizes and shapes (Fig. S4). The size distribution of the synthesized NPs is described in Fig. S5.

The XRD patterns (Fig. 2) show a clear (111) peak at 43.2° for the Cu NPs and at 39.7° for the Pd NPs, which agree well with the reference patterns (JCPDS 01–1242 (Cu) and 01–1310 (Pd)). A Pd atom is much larger than a Cu atom, so the (111) peak shifts to a lower angle as Pd is alloyed into Cu lattice. The (111) peaks of alloy NPs are located between those of pure Pd and Cu NPs. The lack of separate peaks for

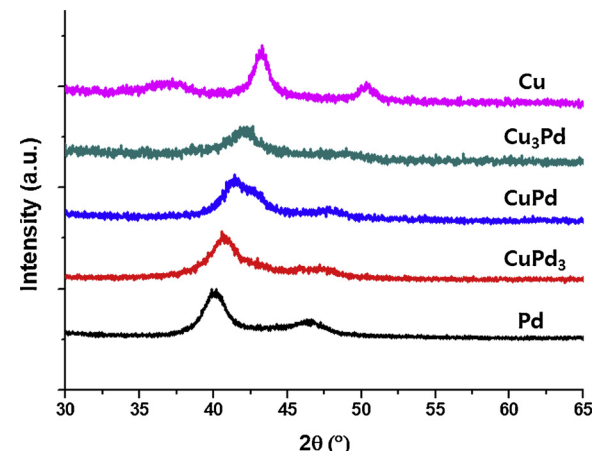
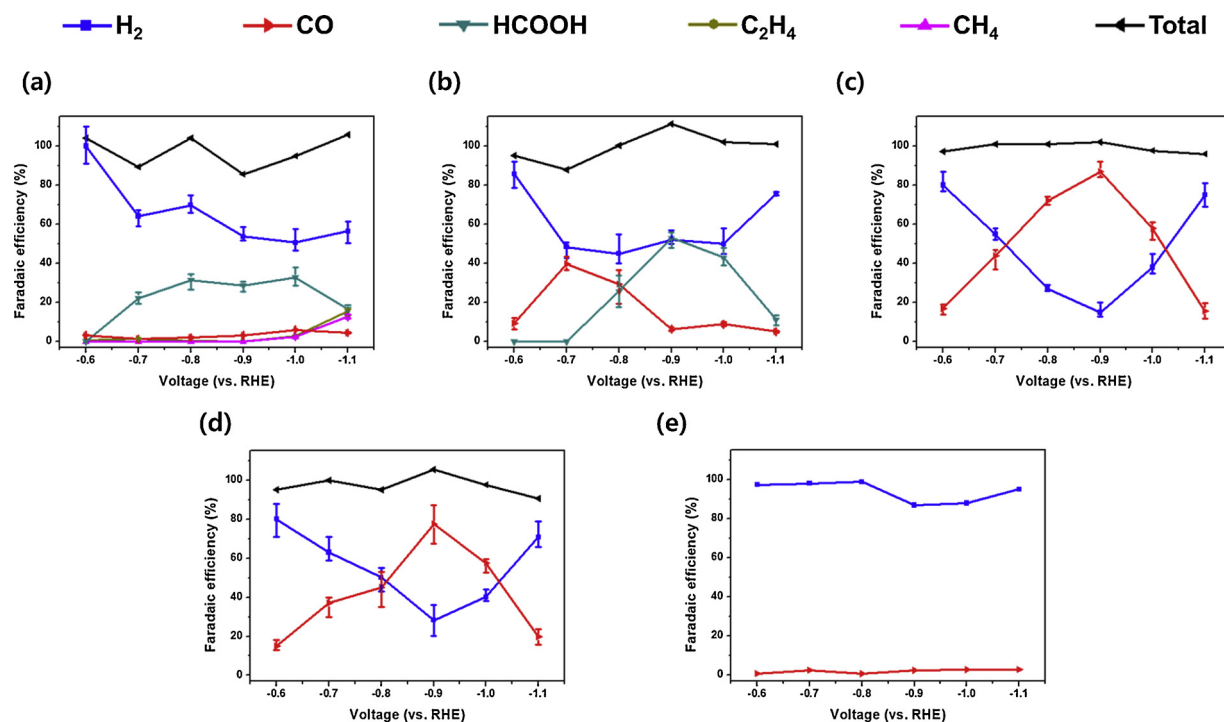


Fig. 2. XRD patterns of Cu NPs, Cu<sub>3</sub>Pd NPs, CuPd NPs, CuPd<sub>3</sub> NPs, and Pd NPs.



**Fig. 3.** Faradaic efficiencies of the Cu-Pd NP/C catalysts in 0.1 M KHCO<sub>3</sub> solution: (a) Cu NP/C, (b) Cu<sub>3</sub>Pd NP/C, (c) CuPd NP/C, (d) CuPd<sub>3</sub> NP/C, and (e) Pd NP/C.

Pd or Cu indicates that they were well mixed as an alloy. The (111) peak positions indicate that the *d*-spacings between (111) planes are 0.214 nm for Cu<sub>3</sub>Pd NPs, 0.218 nm for CuPd NPs, and 0.221 nm for CuPd<sub>3</sub> NPs; these are consistent with the values observed in the HR-TEM images (Fig. S6). We also investigated the distribution of each element in Cu-Pd alloy NPs using STEM-EDS mapping on each Cu-Pd alloy (Fig. S7). The EDS mapping of three samples showed that Cu (yellow) and Pd (blue) atoms were well distributed without forming domains composed of only Pd or Cu.

To use the synthesized NPs as catalysts for CO<sub>2</sub>RR, they were deposited on conductive carbon supports (Vulcan XC-72). The surface capping oleylamine was removed by heat treatment in air at 185 °C. The aggregation or sintering of the NPs did not occur after particle deposition followed by surfactant removal (Fig. S8). The actual compositions (Table S1) of the metal and the loading of metal catalyst on the carbon black were obtained from ICP-OES and TGA measurements.

Electrochemical characterization was performed in CO<sub>2</sub>-purged 0.1 M KHCO<sub>3</sub> solution (Fig. 3). For the preparation of current collectors, a slurry was made by mixing Vulcan XC-72 and PTFE binder (PTFE content: 15 wt%), and this was sprayed onto commercial carbon paper (Toray TGP-H-060). The NPs on carbon were mixed with Nafion ionomer, and the mixture was cast on the current collector by dropping. The electrocatalysis of CO<sub>2</sub> was conducted in a CO<sub>2</sub>-saturated aqueous 0.1 M KHCO<sub>3</sub> solution in a two-compartment cell, which is separated by an anion exchange membrane (Slemion AMV, AGC in Japan). The HER occurred significantly during the electrolysis on the Cu NP/C catalyst (Fig. 3a). Over the whole tested voltage, the FE for H<sub>2</sub> production was greater than 50%. The CO<sub>2</sub>RR produced formic acid, CO, CH<sub>4</sub>, and C<sub>2</sub>H<sub>4</sub>. The FE for formic acid production was relatively higher than those of other products but did not consume a large proportion of the total consumed charge. CO production was detected, but the FE was small enough to be neglected. From -1.0 V, CH<sub>4</sub> and C<sub>2</sub>H<sub>4</sub> were produced, which is a general characteristic of Cu catalysts [17,33,54].

### 3.2. Electrochemical CO<sub>2</sub> reduction on the CuPd alloy nanoparticles

Alloying Pd with Cu caused a significant enhancement in CO<sub>2</sub>RR

catalysis. The CO<sub>2</sub>RR became much more dominant than the HER compared to on Cu NP/C. In particular, the FEs of formic acid and CO production increased drastically, and hydrocarbon (CH<sub>4</sub> and C<sub>2</sub>H<sub>4</sub>) production was totally suppressed. On Cu<sub>3</sub>Pd NP/C, the maximum FE for CO production increased to 43% (at -0.7 V), and the FE for formic acid production was also slightly increased compared to that on Cu NP/C (Fig. 3b). CuPd NP/C had the best catalytic performance for CO<sub>2</sub> conversion to CO among the synthesized alloy NP catalysts. It produced CO as the only product from the CO<sub>2</sub>RR with the maximum FE as high as 87% at -0.9 V vs. RHE (Fig. 3c). Such high selectivity for one gaseous product is advantageous in practical applications because the separation processes become relatively simple. The CuPd<sub>3</sub> NP/C catalyst showed a similar tendency of FE for CO<sub>2</sub>RR to that of CuPd NP/C, but, compared to CuPd/C, it had slightly higher FE for the HER (Fig. 3d). This result is possibly due to the relatively broad size distribution of the CuPd<sub>3</sub> NPs (Fig. S5d). The catalytic activity and selectivity of the NP catalysts for the CO<sub>2</sub>RR were significantly affected by the particle size, shape, and synthesis conditions [21,23,55–57]. Large particles (> 10 nm) occupied a slightly larger fraction of the CuPd<sub>3</sub> NP size distribution than those of the other NPs. The Pd NP/C (Pd NP diameter: 7 nm) catalyst showed almost no activity for CO<sub>2</sub>RR, while the HER was dominant on that catalyst (Fig. 3e). For further comparison of the electrocatalytic behaviors, we synthesized Pd NPs that had average diameters of 4.9 nm (Pd-5 NPs, Fig. S4c) and 3.4 nm (Pd-3 NPs, Fig. S4d). This reduction in the size of the Pd NP catalysts increased the catalytic activity for CO<sub>2</sub>RR. Pd-5 nm achieved a maximum FE for CO production of 54% at -0.8 V, and Pd-3 nm showed maximum FE for CO production of 65% at -0.7 V (Fig. S10a, b).

From a practical viewpoint, the rate at which the specific product is generated is also an important parameter. The CO production current on each catalyst (mass activity normalized by metal catalyst mass [mA mg<sub>catal</sub><sup>-1</sup>] and Pd mass [mA mg<sub>Pd</sub><sup>-1</sup>]) was higher for all the Cu-Pd alloy NP catalysts than the Cu NPs (Fig. 4). The CuPd NP/C catalyst had the highest CO production mass activity of 30 mA mg<sub>catal</sub><sup>-1</sup> at -0.9 V; this activity is one of the highest values among reported metal NP-based catalysts for CO<sub>2</sub>RR (Table S5). When the CO production current was normalized by Pd mass, the mass activity of CuPd NP/C was 49 mA mg<sub>Pd</sub><sup>-1</sup> at -0.9 V, which exceeds those of Pd NP/C, Pd-3 NP/C, Pd-5

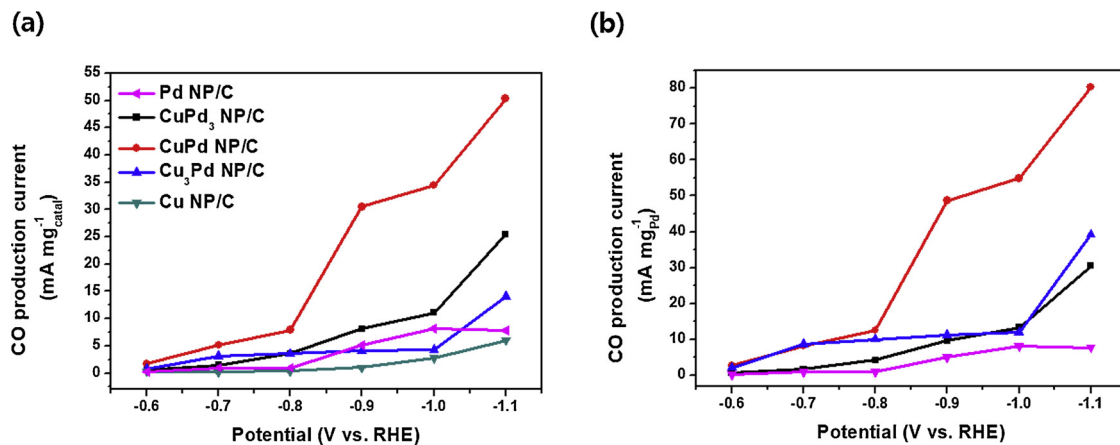


**Fig. 4.** Partial current density of CO production, (a) CO production current normalized by metal mass, and (b) CO production current normalized by noble metal Pd mass.

**Table 1**  
The binding energy of the intermediates on Cu(211) and CuPd(211).

Intermediates	Binding energy (eV)	
	Cu(211)	CuPd(211)
H*	-0.28	-0.40
O*	0.95	1.31
COOH*	1.44	1.39
CO*	1.24	0.57
HCO*	1.58	1.34
COH*	2.14	1.32

**Table 2**  
Limiting potentials at potential-determining steps for each product pathway.

Pathway	Potential-determining step	Cu(211)	CuPd(211)
H <sub>2</sub>	H <sup>*</sup> → H <sub>2</sub>	-0.09 V	-0.21 V
CO	CO <sub>2</sub> (g) + H <sup>+</sup> + e <sup>-</sup> → COOH <sup>*</sup>	-0.41 V	-0.36 V
Hydrocarbon	CO <sup>*</sup> + H <sup>+</sup> + e <sup>-</sup> → HCO <sup>*</sup>	-0.60 V	-1.03 V

from the catalyst surface, which reduces activity toward CO production [39]. The catalytic stability of the CuPd NPs was investigated by continuous electrolysis at -0.9 V in 0.1 M KHCO<sub>3</sub> solution (Fig. S13). As shown in the figure, the CuPd NP/C catalysts displayed superior catalytic stability.

The catalytic behavior of Cu was significantly changed by alloying it with Pd in NP form. Hydrocarbon production was totally suppressed, and CO production with high selectivity and high rate was achieved. The total selectivity for CO<sub>2</sub>RR was also increased as compared to that of Cu NPs. This change to the catalytic properties could be attributed to the change of adsorption properties of the catalyst surface for CO<sub>2</sub>RR intermediates arising from alloying. The adsorption strength of the intermediates on the catalyst is changed by alloying, so the energy barrier to each intermediate step is also changed [33,58]. This feature causes the change of the product and rate of the catalytic reaction. We used a computational technique based on DFT to investigate the changes in adsorption arising from Pd alloying of the Cu catalyst.

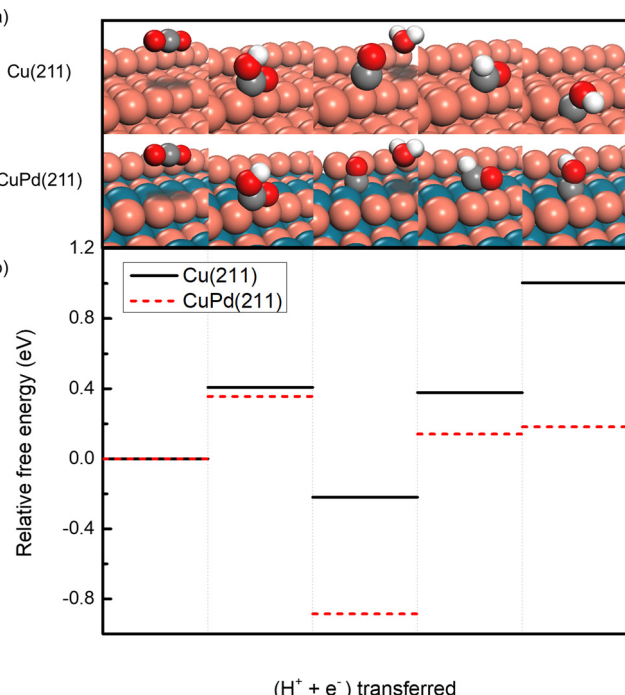


**Fig. 5.** (a) Reaction pathway for CO production on the Cu(211) and CuPd(211) surfaces. (b) Free energy diagram of CO<sub>2</sub>RR on Cu(211) and CuPd(211) surfaces.

NP/C, and the best reported mass activity of Pd NPs for CO production [21] (Fig. S12). This activity enhancement in CuPd alloy is due to weakened binding energy of CO\* intermediate compared to Pd catalysts. On Pd surface, CO\* binding energy is too strong to release CO\*.

### 3.3. Discussion of the effects of alloying using DFT calculations

We employed the (211) stepped surfaces of Cu and CuPd which are known as the active site of electrochemical CO production in Cu and Pd catalysts to model the surface of NP catalysts in DFT calculations [21,59]. Five key adsorption states of COOH\*, CO\*, COH\*, HCO\*, and H\* (where \* indicates an adsorbed state) intermediates were investigated on each catalyst. A starting point of CO<sub>2</sub>RR is the formation of COOH\*, and its stability of which has been considered as a descriptor for the ability of the catalyst to activate CO<sub>2</sub> [28,60]. Meanwhile, HCO\* and COH\* are protonated forms of CO\*. The energy barrier to CO\* protonation often determines the hydrocarbon production from CO<sub>2</sub> on catalyst [28,48,58,61]. In addition, the free energy of hydrogen adsorption is directly correlated with the catalytic behavior for the HER [62]. An investigation of the intermediate states could help to understand how alloying affects the selectivity of CO<sub>2</sub>RR that was observed in the electrochemical characterization.

The binding energies of the CO<sub>2</sub>RR intermediates are more negative on CuPd(211) than on Cu(211), except that of O\*, which is often adsorbed more strongly on 3d-metals than on Pd, Pt, and Au (Table 1).

This strong adsorption of the intermediates on CuPd(211) is attributed to an upshift in the *d*-band center, which was caused by Pd alloying to Cu and the high affinity of Pd to CO<sub>2</sub>RR intermediates [21,28,58]. The Cu atom on CuPd(211) surface has a *d*-band center position closer to the Fermi level than on Cu(211) surface. The calculated *d*-band centers of Cu atoms are -2.13 and -1.60 eV for Cu(211) and CuPd(211), respectively (Fig. S14). As the energy level of the metal *d*-band state interacting with the molecular orbital of adsorbate approaches the Fermi level, the adsorption strength increases. In particular, Pd alloying also induces H\* to be more strongly adsorbed on CuPd(211) than on Cu(211) (Table 1). The calculated binding energy of H\* on Cu(211) is already placed on the left side of the volcano plot which means that stronger adsorption occurs compared to the optimum adsorption for HER [62]. Binding energy of H\* on CuPd(211) is more far from the optimum energy than that of Cu(211), which demonstrates that the HER is less active on CuPd(211) surface. The theoretical calculation agrees well with the experimental measurements of the FE (Fig. 3).

The free energy change of each elementary step is shown in Fig. 5. First, when we focused on the pathway for CO\* formation which is relevant to CO production, the COOH\* formation step is the potential-determining step (PDS) [21]. The limiting potentials in this step are -0.41 V for Cu(211) and -0.36 V for CuPd(211) (Table 2). Although the limiting potential is lower on CuPd(211) than on Cu(211), this difference is < 0.1 eV, which may be too small to explain the selectivity for CO production. Therefore, we additionally considered the next step, CO\* protonation, which is the PDS for hydrocarbon production. HCO\* formation is much more favored than COH\* formation on Cu(211), as reported previously [28,58,61], and on CuPd(211). The limiting potential of the favored CO\* protonation step is much higher on CuPd(211) (-1.03 V) than on Cu(211) (-0.60 V). This difference indicates that hydrocarbon production is less favored on Cu-Pd alloy surface than on a Cu surface. This suppression of hydrocarbon production observed in the electrochemical analysis occurs because the alloying of Cu with Pd causes a considerable increase in the potential of CO\* protonation.

The high limiting potential of CO\* protonation on the CuPd surface may occur because Pd is less oxophilic than Cu. On Cu(211), the highly oxophilic Cu surface interacts with both the C and O atoms of HCO\* (Fig. 5a). This co-interaction stabilizes the adsorbed state of HCO relative to the adsorbed state of CO, so the energy difference between them is small. The small energy barrier of this step induces Cu to produce hydrocarbons from CO<sub>2</sub>.

In contrast, on CuPd(211) only the C atom in HCO\* and COH\* interacts with the surface Pd atom. Because HCO\* has no specific co-interaction effect on the CuPd surface, the free energy difference between the adsorbed state of HCO or COH and the adsorbed state of CO is much larger on CuPd(211) than on Cu(211). This result indicates that the stability of each intermediate state can be selectively controlled by multi-metallic alloying [58]. The fine tuning of the stability of each intermediate state enables the control of the selectivity and the reaction rate of electrochemical CO<sub>2</sub> reduction.

#### 4. Conclusions

We investigated the catalytic effect on alloying Cu with Pd by using monodisperse Cu-Pd NPs of various compositions synthesized by a colloidal method. Alloying Pd to Cu in NPs suppressed hydrocarbon production and greatly increased CO production to one of the highest values of noble metal mass activity for CO production achieved to date. DFT results suggest that alloying Pd to Cu increases the energy barrier of the CO protonation step, which is the potential-determining step for hydrocarbon production, causing a selectivity change in CO<sub>2</sub>RR. This is the first report that has used both electrochemical analysis and the theoretical limiting potential of the CO\* protonation step to explain the suppression of hydrocarbon production on Cu alloy catalysts. Both experimental and computational results show that bimetallic alloying can control the selectivity of the catalyst for CO<sub>2</sub>RR by changing the

stability of each intermediate selectively. The series of Cu-Pd NPs indicates that combining a well-designed alloyed surface and nanostucture can yield a desirable CO<sub>2</sub>RR catalyst with high production rate and high selectivity in the aqueous phase.

#### Acknowledgments

This research was supported by the Korea Institute of Energy Technology Evaluation and Planning (KETEP) and the Ministry of Trade, Industry & Energy (MOTIE) of the Republic of Korea (No. 20174030201600 and No. 20182010600430) and the National Research Foundation of Korea (NRF) funded by the Ministry of Science and ICT (2018M3D3A1A01018005 and 2018M1A2A2061987).

#### Appendix A. Supplementary data

Supplementary material related to this article can be found, in the online version, at doi:<https://doi.org/10.1016/j.apcatb.2019.01.021>.

#### References

- [1] S.H. Schneider, The greenhouse effect: science and policy, *Science* 243 (1989) 771–781.
- [2] M.S. Dresselhaus, I.L. Thomas, Alternative energy technologies, *Nature* 414 (2001) 332–337.
- [3] D. Larcher, J.M. Tarascon, Towards greener and more sustainable batteries for electrical energy storage, *Nat. Chem.* 7 (2015) 19–29.
- [4] N.S. Lewis, D.G. Nocera, Powering the planet: chemical challenges in solar energy utilization, *Proc. Natl. Acad. Sci. U. S. A.* 103 (2006) 15729–15735.
- [5] G. Centi, E.A. Quadrelli, S. Perathoner, Catalysis for CO<sub>2</sub> conversion: a key technology for rapid introduction of renewable energy in the value chain of chemical industries, *Energy Environ. Sci.* 6 (2013) 1711–1731.
- [6] R.S. Haszeldine, Carbon capture and storage: how green can black be? *Science* 325 (2009) 1647–1652.
- [7] M. Aresta, A. Dibenedetto, A. Angelini, Catalysis for the valorization of exhaust carbon: from CO<sub>2</sub> to chemicals, materials, and fuels. technological use of CO<sub>2</sub>, *Chem. Rev.* 114 (2014) 1709–1742.
- [8] E.V. Kondratenko, G. Mul, J. Baltrusaitis, G.O. Larrazabal, J. Perez-Ramirez, Status and perspectives of CO<sub>2</sub> conversion into fuels and chemicals by catalytic, photocatalytic and electrocatalytic processes, *Energy Environ. Sci.* 6 (2013) 3112–3135.
- [9] L.R. Winter, E. Gomez, B.H. Yan, S.Y. Yao, J.G.G. Chen, Tuning Ni-catalyzed CO<sub>2</sub> hydrogenation selectivity via Ni-ceria support interactions and Ni-Fe bimetallic formation, *Appl. Catal. B* 224 (2018) 442–450.
- [10] L.J. Liu, C.Y. Zhao, J.Y. Xu, Y. Li, Integrated CO<sub>2</sub> capture and photocatalytic conversion by a hybrid adsorbent/photocatalyst material, *Appl. Catal. B* 179 (2015) 489–499.
- [11] K.M. Yu, I. Curcic, J. Gabriel, S.C. Tsang, Recent advances in CO<sub>2</sub> capture and utilization, *ChemSusChem* 1 (2008) 893–899.
- [12] P. Markewitz, W. Kuckshinrichs, W. Leitner, J. Linssen, P. Zapp, R. Bongartz, A. Schreiber, T.E. Müller, Worldwide innovations in the development of carbon capture technologies and the utilization of CO<sub>2</sub>, *Energy Environ. Sci.* 5 (2012) 7281.
- [13] J. Liu, C. Guo, A. Vasileff, S. Qiao, Nanostructured 2D materials: prospective catalysts for electrochemical CO<sub>2</sub> reduction, *Small Methods* 1 (2017) 1600006.
- [14] M. Mikkelsen, M. Jorgensen, F.C. Krebs, The teraton challenge. a review of fixation and transformation of carbon dioxide, *Energy Environ. Sci.* 3 (2010) 43–81.
- [15] D.D. Zhu, J.L. Liu, S.Z. Qiao, Recent advances in inorganic heterogeneous electro-catalysts for reduction of carbon dioxide, *Adv. Mater.* 28 (2016) 3423–3452.
- [16] H.-R.M. Jhong, S. Ma, P.J.A. Kenis, Electrochemical conversion of CO<sub>2</sub> to useful chemicals: current status, remaining challenges, and future opportunities, *Curr. Opin. Chem. Eng.* 2 (2013) 191–199.
- [17] K.P. Kuhl, E.R. Cave, D.N. Abram, T.F. Jaramillo, New insights into the electrochemical reduction of carbon dioxide on metallic copper surfaces, *Energy Environ. Sci.* 5 (2012) 7050–7059.
- [18] A. Vasileff, Y. Zheng, S.Z. Qiao, Carbon solving carbon's problems: recent progress of nanostructured carbon-based catalysts for the electrochemical reduction of CO<sub>2</sub>, *Adv. Energy Mater.* 7 (2017) 1700759.
- [19] J. Liu, C. Guo, A. Vasileff, S. Qiao, Nanostructured 2D materials: prospective catalysts for electrochemical CO<sub>2</sub> reduction, *Small Methods* 1 (2017) 1600006.
- [20] Y. Chen, M.W. Kanan, Tin oxide dependence of the CO<sub>2</sub> reduction efficiency on tin electrodes and enhanced activity for tin/tin oxide thin-film catalysts, *J. Am. Chem. Soc.* 134 (2012) 1986–1989.
- [21] D. Gao, H. Zhou, J. Wang, S. Miao, F. Yang, G. Wang, J. Wang, X. Bao, Size-dependent electrocatalytic reduction of CO<sub>2</sub> over Pd nanoparticles, *J. Am. Chem. Soc.* 137 (2015) 4288–4291.
- [22] C. Kim, H.S. Jeon, T. Eom, M.S. Jee, H. Kim, C.M. Friend, B.K. Min, Y.J. Hwang, Achieving selective and efficient electrocatalytic activity for CO<sub>2</sub> reduction using immobilized silver nanoparticles, *J. Am. Chem. Soc.* 137 (2015) 13844–13850.
- [23] W. Zhu, R. Michalsky, Ö. Metin, H. Lv, S. Guo, C.J. Wright, X. Sun, A.A. Peterson, S. Sun, Monodisperse Au nanoparticles for selective electrocatalytic reduction of

CO<sub>2</sub> to CO, *J. Am. Chem. Soc.* 135 (2013) 16833–16836.

[24] Y.S. Ham, S. Choe, M.J. Kim, T. Lim, S.-K. Kim, J.J. Kim, Electrodeposited Ag catalysts for the electrochemical reduction of CO<sub>2</sub> to CO, *Appl. Catal. B* 208 (2017) 35–43.

[25] Q. Lu, J. Rosen, Y. Zhou, G.S. Hutchings, Y.C. Kimmel, J.G. Chen, F. Jiao, A selective and efficient electrocatalyst for carbon dioxide reduction, *Nat. Commun.* 5 (2014) 3242.

[26] Y. Jiao, Y. Zheng, P. Chen, M. Jaroniec, S.Z. Qiao, Molecular scaffolding strategy with synergistic active centers to facilitate electrocatalytic CO<sub>2</sub> reduction to hydrocarbon/alcohol, *J. Am. Chem. Soc.* 139 (2017) 18093–18100.

[27] R. Aydin, H.O. Dogan, F. Koleli, Electrochemical reduction of carbondioxide on polypyrrole coated copper electro-catalyst under ambient and high pressure in methanol, *Appl. Catal. B* 140 (2013) 478–482.

[28] A.A. Peterson, J.K. Nørskov, Activity descriptors for CO<sub>2</sub> electroreduction to methane on transition-metal catalysts, *J. Phys. Chem. Lett.* 3 (2012) 251–258.

[29] V.R. Stamenkovic, B.S. Mun, M. Arenz, K.J.J. Mayrhofer, C.A. Lucas, G. Wang, P.N. Ross, N.M. Markovic, Trends in electrocatalysis on extended and nanoscale Pt-bimetallic alloy surfaces, *Nat. Mater.* 6 (2007) 241–247.

[30] J.A. Rodriguez, D.W. Goodman, The nature of the metal–metal bond in bimetallic surfaces, *Science* 257 (1992) 897–903.

[31] M. Mavrikakis, B. Hammer, J.K. Nørskov, Effect of strain on the reactivity of metal surfaces, *Phys. Rev. Lett.* 81 (1998) 2819–2822.

[32] J.R. Kitchin, J.K. Nørskov, M.A. Bartaeu, J.G. Chen, Modification of the surface electronic and chemical properties of Pt(111) by subsurface 3d transition metals, *J. Chem. Phys.* 120 (2004) 10240–10246.

[33] D. Kim, J. Resasco, Y. Yu, A.M. Asiri, P. Yang, Synergistic geometric and electronic effects for electrochemical reduction of carbon dioxide using gold–copper bimetallic nanoparticles, *Nat. Commun.* 5 (2014) 4948.

[34] C.W. Lee, K.D. Yang, D. Nam, J.H. Jang, N.H. Cho, S.W. Im, K.T. Nam, Defining a materials database for the design of copper binary alloy catalysts for electrochemical CO<sub>2</sub> conversion, *Adv. Mater.* 30 (2018) 1706617.

[35] S. Guo, S. Zhang, S. Sun, Tuning nanoparticle catalysis for the oxygen reduction reaction, *Angew. Chem. Int. Ed.* 52 (2013) 8526–8544.

[36] Z. Peng, H. Yang, Designer platinum nanoparticles: control of shape, composition in alloy, nanostructure and electrocatalytic property, *Nano Today* 4 (2009) 143–164.

[37] J. Park, J. Joo, S.G. Kwon, Y. Jang, T. Hyeon, Synthesis of monodisperse spherical nanocrystals, *Angew. Chem. Int. Ed.* 46 (2007) 4630–4660.

[38] S. Ma, M. Sadakiyo, M. Heima, R. Luo, R.T. Haasch, J.I. Gold, M. Yamauchi, P.J.A. Kenis, Electrocatalysis of carbon dioxide to hydrocarbons using bimetallic Cu–Pd catalysts with different mixing patterns, *J. Am. Chem. Soc.* 139 (2017) 47–50.

[39] Z. Yin, D.F. Gao, S.Y. Yao, B. Zhao, F. Cai, L.L. Lin, P. Tang, P. Zhai, G.X. Wang, D. Ma, X.H. Bao, Highly selective palladium–copper bimetallic electrocatalysts for the electrochemical reduction of CO<sub>2</sub> to CO, *Nano Energy* 27 (2016) 35–43.

[40] Z.P. Jovanov, H.A. Hansen, A.S. Varela, P. Malacrida, A.A. Peterson, J.K. Nørskov, I.E.L. Stephens, I. Chorkendorff, Opportunities and challenges in the electrocatalysis of CO<sub>2</sub> and CO reduction using bifunctional surfaces: a theoretical and experimental study of Au–Cd alloys, *J. Catal.* 343 (2016) 215–213.

[41] J. Greeley, T.F. Jaramillo, J. Bonde, I. Chorkendorff, J.K. Nørskov, Computational high-throughput screening of electrocatalytic materials for hydrogen evolution, *Nat. Mater.* 5 (2006) 909–913.

[42] S.-W. Kim, J. Park, Y. Jang, Y. Chung, S. Hwang, T. Hyeon, Y.W. Kim, Synthesis of monodisperse palladium nanoparticles, *Nano Lett.* 3 (2003) 1289–1291.

[43] S.U. Son, I.K. Park, J. Park, T. Hyeon, Synthesis of Cu<sub>2</sub>O coated Cu nanoparticles and their successful applications to Ullmann-type amination coupling reactions of aryl chlorides, *Chem. Commun.* (2004) 778–779.

[44] P.E. Blöchl, Projector augmented-wave method, *Phys. Rev. B* 50 (1994) 17953–17979.

[45] G. Kresse, J. Furthmüller, Efficient iterative schemes for ab initio total-energy calculations using a plane-wave basis set, *Phys. Rev. B* 54 (1996) 11169–11186.

[46] G. Kresse, J. Hafner, Ab initio molecular dynamics for liquid metals, *Phys. Rev. B* 47 (1993) 558–561.

[47] D.S. Sholl, J.A. Steckel, *Density Functional Theory: a Practical Introduction*, John Wiley & Sons, Inc., 2009.

[48] J.P. Perdew, K. Burke, M. Ernzerhof, Generalized gradient approximation made simple, *Phys. Rev. Lett.* 77 (1996) 3865–3868.

[49] M. Methfessel, A.T. Paxton, High-precision sampling for Brillouin-zone integration in metals, *Phys. Rev. B* 40 (1989) 3616–3621.

[50] A.A. Peterson, F. Abild-Pedersen, F. Studt, J. Rossmeisl, J.K. Nørskov, How copper catalyzes the electroreduction of carbon dioxide into hydrocarbon fuels, *Energy Environ. Sci.* 3 (2010) 1311–1315.

[51] J.K. Nørskov, J. Rossmeisl, A. Logadottir, L. Lindqvist, J.R. Kitchin, T. Bligaard, H. Jónsson, Origin of the overpotential for oxygen reduction at a fuel-cell cathode, *J. Phys. Chem. B* 108 (2004) 17886–17892.

[52] M. Fishman, H.L. Zhuang, K. Mathew, W. Dirschna, R.G. Hennig, Accuracy of exchange-correlation functionals and effect of solvation on the surface energy of copper, *Phys. Rev. B* 87 (2013) 245402.

[53] Q. Gao, Y.-M. Ju, D. An, M.-R. Gao, C.-H. Cui, J.-W. Liu, H.-P. Cong, S.-H. Yu, Shape-controlled synthesis of monodisperse PdCu nanocubes and their electrocatalytic properties, *ChemSusChem* 6 (2013) 1878–1882.

[54] C.W. Li, M.W. Kanan, CO<sub>2</sub> reduction at low overpotential on Cu electrodes resulting from the reduction of thick Cu<sub>2</sub>O films, *J. Am. Chem. Soc.* 134 (2012) 7231–7234.

[55] R. Reske, H. Mistry, F. Behafard, B. Roldan Cuenya, P. Strasser, Particle size effects in the catalytic electroreduction of CO<sub>2</sub> on Cu nanoparticles, *J. Am. Chem. Soc.* 136 (2014) 6978–6986.

[56] S. Liu, H. Tao, L. Zeng, Q. Liu, Z. Xu, Q. Liu, J.L. Luo, Shape-dependent electrocatalytic reduction of CO<sub>2</sub> to CO on triangular silver nanoplates, *J. Am. Chem. Soc.* 139 (2017) 2160–2163.

[57] H. Huang, H. Jia, Z. Liu, P. Gao, J. Zhao, Z. Luo, J. Yang, J. Zeng, Understanding of strain effects in the electrochemical reduction of CO<sub>2</sub>: using Pd nanostructures as an ideal platform, *Angew. Chem. Int. Ed.* 56 (2017) 3594–3598.

[58] H.A. Hansen, C. Shi, A.C. Lausche, A.A. Peterson, J.K. Nørskov, Bifunctional alloys for the electroreduction of CO<sub>2</sub> and CO, *Phys. Chem. Chem. Phys.* 18 (2016) 9194–9201.

[59] W.J. Durand, A.A. Peterson, F. Studt, F. Abild-Pedersen, J.K. Nørskov, Structure effects on the energetics of the electrochemical reduction of CO<sub>2</sub> by copper surfaces, *Surf. Sci.* 605 (2011) 1354–1359.

[60] H.-K. Lim, H. Shin, W.A. Goddard, Y.J. Hwang, B.K. Min, H. Kim, Embedding covalency into metal catalysts for efficient electrochemical conversion of CO<sub>2</sub>, *J. Am. Chem. Soc.* 136 (2014) 11355–11361.

[61] T. Adit Maark, B.R.K. Nanda, CO and CO<sub>2</sub> electrochemical reduction to methane on Cu, Ni, and Cu<sub>3</sub>Ni (211) surfaces, *J. Phys. Chem. C* 120 (2016) 8781–8789.

[62] J. Greeley, T.F. Jaramillo, J. Bonde, I. Chorkendorff, J.K. Nørskov, Computational high-throughput screening of electrocatalytic materials for hydrogen evolution, *Nat. Mater.* 5 (2006) 909–913.